Fault structure, stress, or pressure control of the seismicity in shale? Insights from a controlled experiment of fluid-induced fault reactivation

L. de Barros, G. Daniel, Y. Guglielmi, D. Rivet, H. Caron, X. Payre, G. Bergery, P Henry, R. Castilla, P. Dick, et al.

AGU PUBLICATIONS

JGR

Journal of Geophysical Research: Solid Earth

RESEARCH ARTICLE
10.1002/2015JB012633

Key Points:
- A natural fault in shale was reactivated by fluid injection in a controlled experiment
- Most of the deformation is aseismic, but a sparse seismicity was recorded
- Seismicity occurs on calcified structures, and its distribution depends on the fault architecture

Correspondence to:
L. De Barros,
louis.debarros@geoazur.unice.fr

Citation:
De Barros, L., et al. (2016), Fault structure, stress, or pressure control of the seismicity in shale? Insights from a controlled experiment of fluid-induced fault reactivation, *J. Geophys. Res. Solid Earth*, *121*, 4506–4522, doi:10.1002/2015JB012633.

Received 30 OCT 2015
Accepted 3 JUN 2016
Accepted article online 6 JUN 2016
Published online 27 JUN 2016

Fault structure, stress, or pressure control of the seismicity in shale? Insights from a controlled experiment of fluid-induced fault reactivation

Louis De Barros[1], Guillaume Daniel[2], Yves Guglielmi[3], Diane Rivet[1], Hervé Caron[4], Xavier Payre[5], Guillaume Bergery[5], Pierre Henry[3], Raymi Castilla[5], Pierre Dick[6], Ernesto Barbieri[2], and Maxime Gourlay[2]

[1]GEOAZUR, University of Nice Sophia-Antipolis, CNRS, IRD, Côte d'Azur Observatory, Sophia Antipolis, France, [2]MAGNITUDE, Centre Regain-Route de Marseille, Sainte-Tulle, France, [3]CEREGE, Aix-Marseille University, CNRS, IRD, Marseille, France, [4]SITES S.A.S., Espace Européen, Ecully, France, [5]TOTAL, Exploration and Production, Research and Development, Pau cedex, France, [6]IRSN, Laboratoire d'Etude et de Recherche sur les Transferts et les Interactions dans les Sols, Fontenay-aux-Roses, France

Abstract Clay formations are present in reservoirs and earthquake faults, but questions remain on their mechanical behavior, as they can vary from ductile (aseismic) to brittle (seismic). An experiment, at a scale of 10 m, aims to reactivate a natural fault by fluid pressure in shale materials. The injection area was surrounded by a dense monitoring network comprising pressure, deformation, and seismicity sensors, in a well-characterized geological setting. Thirty-two microseismic events were recorded during several injection phases in five different locations within the fault zone. Their computed magnitude ranged between −4.3 and −3.7. Their spatiotemporal distribution, compared with the measured displacement at the injection points, shows that most of the deformation induced by the injection is aseismic. Whether the seismicity is controlled by the fault architecture, mineralogy of fracture filling, fluid, and/or stress state is then discussed. The fault damage zone architecture and mineralogy are of crucial importance, as seismic slip mainly localizes on the sealed-with-calcite fractures which predominate in the fault damage zone. As no seismicity is observed in the close vicinity of the injection areas, the presence of fluid seems to prevent seismic slips. The fault core acts as an impermeable hydraulic barrier that favors fluid confinement and pressurization. Therefore, the seismic behavior seems to be strongly sensitive to the structural heterogeneity (including permeability) of the fault zone, which leads to a heterogeneous stress response to the pressurized volume.

1. Introduction

Shale and clay-rich formations are abundant in the Earth's subsurface. Understanding their hydromechanical properties and the behavior of faults within these materials is of crucial importance to better appreciate fluid migration in deep sedimentary basins, earthquake sources, and the potential loss of integrity of geological barriers. For example, the production of shale gas strongly increased in the last decade. On the one hand, because of the low permeability of these reservoirs, production requires hydraulic pressurization so as to increase their permeability by opening new fractures and/or inducing slip on preexisting faults [*Zoback*, 2010]. The reservoir performance in shale formations therefore depends on how efficiently the fracturing can be induced [e.g., *Andersen et al.,* 2013; *Bodziak et al.,* 2014]. On the other hand, when fracturing the shale, large existing faults may also be reactivated, leading to sharp changes in the reservoir behavior and even triggering large earthquakes, which can be damaging for the surrounding areas (see *Davies et al.* [2013] for a review paper) [*Rutqvist et al.,* 2013]. Similarly, the integrity of hydrocarbon reservoirs [*Ingram and Urai*, 1999] or of gas/CO_2 deep geological storage [*Mazzoldi et al.,* 2012] requires that pressure changes inside porous reservoirs should be restricted to prevent slips on existing fractures or faults in the impermeable cap rock. An increase of permeability by several orders of magnitude, and therefore leaks from the reservoirs, might otherwise occur. Moreover, some seismogenic faults have been shown to contain a significant amount of clay-rich materials, particularly in their gouge zone [*Faulkner et al.,* 2011; *Ikari et al.,* 2009; *Carpenter et al.,* 2011; *Bullock et al.,* 2015]. These materials have been recognized to be present on the slip surface and to play a major role in the earthquake sources [e.g., *Imber et al.,* 2008; *Heermance et al.,* 2003]. Indeed, they strongly modify the fault zone behavior by affecting its frictional properties. If the influence of clay-rich minerals on the friction is not taken into account, our understanding of the seismic cycle might be oversimplified, as earthquakes do not nucleate but easily propagate on such faults [*Faulkner et al.,* 2011].

Despite its crucial importance, the hydromechanical behavior of clay formations is still not fully understood. The main reason is the wide variety of behavior observed for these materials, as observed by numerous studies at laboratory scale. Frictional strength depends on mineralogy composition, clay type, and microstructural organization, temperature, pressure, and water content [*Moore and Lockner*, 2004; *Saffer and Marone*, 2003; *Den Hartog and Spiers*, 2013; *Ikari et al.,* 2009; *Kohli and Zoback*, 2013; *Bullock et al.,* 2015; *Tesei et al.,* 2014]. Failure can vary from ductile (stable and aseismic) to brittle and seismic. However, small samples (sometimes made of synthetic mixtures) are not necessarily representative of the full complexity and heterogeneity of a natural fault [e.g., *Bullock et al.,* 2015], which in the field appears as a thick zone with a complex architecture with materials ranging from fractured rocks to gouge. The strong anisotropy and complex fracturing, inherited from the geological history, can significantly affect its mechanical behavior. Furthermore, the hydromechanical context usually lacks resolution at the fault scale [e.g., *Andersen et al.,* 2013; *Das and Zoback*, 2013a, 2013b]. Therefore, how faulted clay-rich formations accommodate deformation in both reservoirs and tectonic fault zones is still an open question.

It is fundamental to understand how the deformation is expressed seismically, as microseismic activity is among the rare probes able to monitor the hydromechanical state of a reservoir or a fault zone. In some cases, microseismicity is a good indicator of the fluid diffusion within the medium and a reliable proxy to fault activation at depth. The clustering of events around the pressurized zone can then be used as an efficient monitoring tool [e.g., *Shapiro and Dinske*, 2009]. In other cases, no or only a few seismic events are recorded despite evidence of significant deformation, which is therefore interpreted as aseismic. Recently, intermediate types of seismicity have been observed in tectonic zones [e.g., *Peng and Gomberg*, 2010], in a controlled fault reactivation experiment [*Derode et al.,* 2015] and in shale reservoirs [*Das and Zoback,* 2013a, 2013b; *Zecevic et al.,* 2016]. These seismic signatures, called tremors or long-period long duration events, are interpreted as slow velocity slips on large fault patches. They could fill the gap between the fast, seismic slip, and the slow, aseismic deformation [*Peng and Gomberg*, 2010]. Fault slips in clay-rich materials can therefore have very different signatures, from totally aseismic to seismic. This makes it challenging to use microseismicity to monitor fault slip and to infer deformation and mechanical processes from it. The aim of this study is therefore to investigate how seismicity occurs and what factors control seismic emissions in clay formations.

For this study, we designed a unique injection experiment where both injection pressure and flow rate were fully controlled, at an intermediate scale, i.e., with a typical length of a few meters [*Guglielmi et al.,* 2015a]. The experiment is performed in a faulted shale layer, which was accessed by short boreholes (approximately 20 to 30 m long) from a tunnel at 270 m depth below the surface. A dense network of sensors recording fluid pressure, flow rate, deformation, and seismic activity monitors the shale responses. In this article, we will analyze the seismic events induced along preexisting faults in a shale material in order to understand the controlling factor of the seismicity in a well-known geological and hydromechanical setting. After a description of the geology, we will focus on the injection experiment and the monitoring system. Although only a few microseismic events were recorded during this experiment, we provide a detailed analysis of their characteristics (location, mechanism, and spectral properties). In addition, their source properties are confronted with observations made of fault architecture, mineralogy, fluid pressure, and stress state. Regardless of the small number of events (revealing that most of the deformation is aseismic), clear evidence can be inferred on the controlling factors of the seismic activity in shale.

2. Geological Context

The experiment took place in the Institute of Radio-Protection and Nuclear Safety (IRSN) underground research laboratory of Tournemire, located in the southwest of France. This former railway tunnel crosscuts a 250 m thick Toarcian shales formation at a depth of 270 m below the topographic surface. The shale composition is relatively homogeneous with more than 50 wt % of phyllosilicates, 15–20 wt % of quartz, and 15–20 wt % of carbonates [*Tremosa et al.,* 2012]. The clay minerals are mainly illite and illite-smectite mixed layers, with 10–15% of kaolinite and less than 5% of chlorite [*Charpentier et al*., 2003]. Its porosity is 10–13% with a 10^{-15} to 10^{-11} m/s permeability (i.e., 0.1 to 1000 nanodarcy). The bedding is subhorizontal to 5–10° dipping to the north, with typical anisotropic properties induced by compaction processes. A kilometric-scale complex network of faults [*Constantin et al.,* 2004] is visible in the shale layer from the tunnel boreholes and from the adjacent galleries.

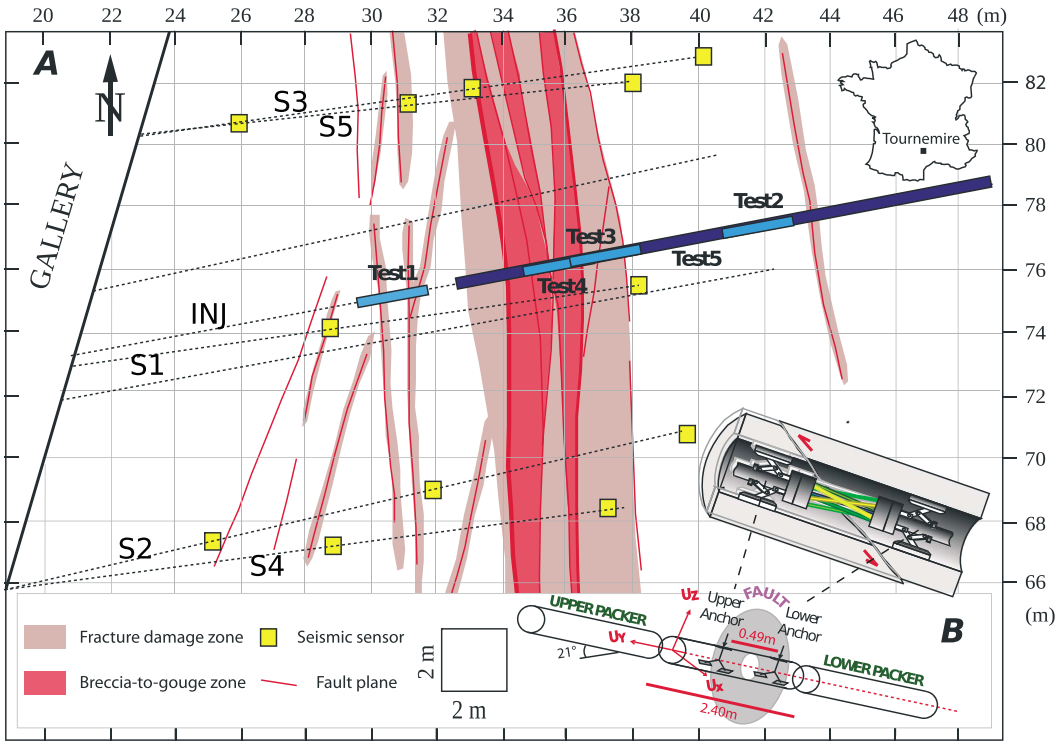

Figure 1. (a) Map view of the experiment zone. The dotted lines show the boreholes. Accelerometric sensors (yellow squares) are cemented into boreholes (dotted lines) named S2, S4, S1, S3, and S5. Main features of the fault zone, inferred from observations from the borehole logs, are schematically drawn in red (gouge zone) and purple (damage zone). The red lines represent the main fractures. The injection areas, from the INJ borehole, are represented as blue rectangles (light blue for tests 1 to 4, dark blue for test 5). (b) Schematic plan of the SIMFIP probe showing the location of the displacement measuring cage in the injection chamber isolated by the straddle packers and a detail of the cage with its upper and lower anchors.

The injection experiment aims at testing the hydromechanical and seismological response of one of these faults, which is an N0, 70–80°W left-lateral strike-slip fault, with a vertical offset estimated at 5 to 6 m [*Dick et al.,* 2015]. In the experiment zone (see Figure 1), the fault is located at a horizontal distance of 10 to 20 m from the tunnel wall. Eight boreholes drilled for the experiment intersect the fault zone, which is approximately 8.5 m thick. The fault core is 2.5 m thick on average [*Guglielmi et al.,* 2015b; *Lefevre*, 2016]. It can be identified as it is bounded on both sides by two main fault surfaces, N150–180, 60–80°W. The core is composed of different deformed materials: shale formation split into small slivers, thin shear zones filled by gouge materials, breccia, and highly fractured to almost intact (but rotated) shale blocks. The fault damage zone is also very heterogeneous and asymmetric, with an average extent of 4.5 m in the western compartment and only 1.75 m on the eastern side.

On both sides of the fault, the damage zone mainly contains N150–180, 30–60°W structures (Family 1), most of them being sealed with calcite veins. On average, most of these structures are of short extent (<1 m), as they do not correlate between adjacent boreholes. On the western hanging wall, in addition to the Family 1 structures, subvertical secondary faults (N160–200°, Family 2) are several meters long and are not sealed with calcite. Bedding in the hanging wall appears folded close to some secondary structures and at the boundary with the fault core. This generates planes with a subhorizontal to 20°N dip with slickenlines showing a reverse or normal movement and a partial calcite sealing (Family 3) [*Lefevre*, 2016].

The stress state was determined by *Cornet* [2000] with a series of leak-off tests performed in a ~180 m deep vertical borehole at different depths (to estimate stress variations with depth) and located ~50 m from the current experiment. Leak-off tests show a strike-slip regime with a stress regime of $\sigma_1 = 4 \pm 2$ MPa, horizontal and oriented N162° ± 15°E, $\sigma_2 = 3.8 \pm 0.4$ MPa which roughly corresponds to the weight of the overburden, inclined 7–8° from the vertical in the N72° direction and $\sigma_3 = 2.1 \pm 1$ MPa, inclined 7–8° from the horizontal in the N72° direction.

3. Methods: Experiment and Analysis

3.1. Injection Probe

The injection borehole is 30 m long, dipping 20°E. The injection was done with a probe named step-rate injection method for fracture in situ properties (SIMFIP), described in detail by *Guglielmi et al.* [2013]. This probe allows characterizing the hydromechanical response of specific narrow zones or individual fractures alone. A straddle packer system isolates a 2.4 m long injection chamber in the borehole (Figure 1b). Inside this chamber, a three-directional extensometer, based on optic fiber Bragg gratings, measures precisely the borehole wall displacements (resolution of 0.1 μm). This sensor is coupled to the borehole wall independently from the straddle packer system by two anchoring systems located on both sides of a 0.5 m long zone containing the tested fractures. Relative motion on these fractures produces a deformation of a set of six metallic tubes with various orientations that connect the two anchoring systems. The deformation of these tubes is then monitored through optic fibers. An inversion algorithm is later used to calculate the 3-D displacement of the upper anchor relative to the lower one, which is considered fixed. A pressure sensor located in the injection chamber, with an accuracy of 0.001 MPa, can capture small pressure variations related to fracture movement.

In the tunnel, the pumping systems produce controlled injection pressures up to 6 MPa for varying time durations. The flow rate is directly measured at the pump by a turbine flow meter, in the 1–100 L/min range, with a 0.1 L/min accuracy. All the data (deformation, pressure, and flow rate) are transmitted to the acquisition system which continuously records at a sampling rate of 1 kHz. From the hydromechanical data, we will infer the failures determined by (1) an increase of flow rate without an increase of pressure and (2) a change in the deformation direction. We refer the reader to *Guglielmi et al.* [2013] for a detailled description of the probe and the injection method.

Five different series of injections at pressures up to 4.6 MPa were performed on different locations within the fault zone, following the protocol defined by *Guglielmi et al.* [2013]. Inside each series, named tests 1 to 5 (see Figure 2 and Table 1), several cycles of injection, with different lengths and pressure, were used. The in-depth analysis of the hydromechanical responses of the individual cycles is, however, beyond the scope of this paper (see *Guglielmi et al.* [2015b] for test 1). Tests 1 to 4 were performed in a 2.4 m long injection chamber located on different structures of the fault zone (Figure 1 and Table 1). In test 5, only one packer was used to allow a larger injection zone, from 1 m west of the fault core to its end, i.e., including a 1 m long part of the western damage zone, the fault core, and the eastern damage zone. This test aims to stimulate the whole fault zone simultaneously. Only the large secondary faults on the west damage zone were not included. The injection method is the same as for tests 1 to 4, except that no deformation measurements could be performed.

3.2. Seismic Monitoring

The area where injections were performed was surrounded by a network of 12 triaxial accelerometers at short distances (between 4 and 12 m), in order to capture the induced seismic emissions with the highest precision. These sensors were cemented in five different boreholes named S1 to S5 (see Figure 1). Two boreholes, dipping subhorizontally (S3, three sensors) and 40°E (S5, two sensors) are located at about 7.5 m north of the injection area. Two other boreholes (S2 and S4), with similar orientation and sensors as respectively S3 and S5, are located symmetrically 7.5 m south of the injection area. The last borehole (S1), dipping 20°E, is roughly parallel to the injection borehole at a distance of approximately 50 cm. Note that in each borehole, sensors were deployed on both sides of the fault zone. All the monitoring boreholes surrounding the injection were cemented; they had a limited influence on the stress state or on the fluid diffusivity.

As the injected volume was planned to be small compared to industrial injection, it was anticipated that potential induced microearthquakes would have small magnitudes and high-frequency contents. Sensors were thus selected to have broad- and high-frequency responses. Three-component accelerometers (PCB 356B18, flat response 2 Hz–4 kHz) were preferred to geophones, as the latter cannot give a correct response at high frequency (i.e., above 1 kHz). On-site comparison shows that accelerometers are more sensitive than geophones above a frequency of approximately 250 Hz. The acceleration data were continuously recorded with a 10 kHz sampling frequency by the acquisition system (Gantner instrument), which allows the synchronous record synchronously of different sensor types (deformation, pressure, acceleration, etc.) at different sampling frequencies. Seismic events were detected and located from the continuous data, and their mechanisms and spectral properties were then computed.

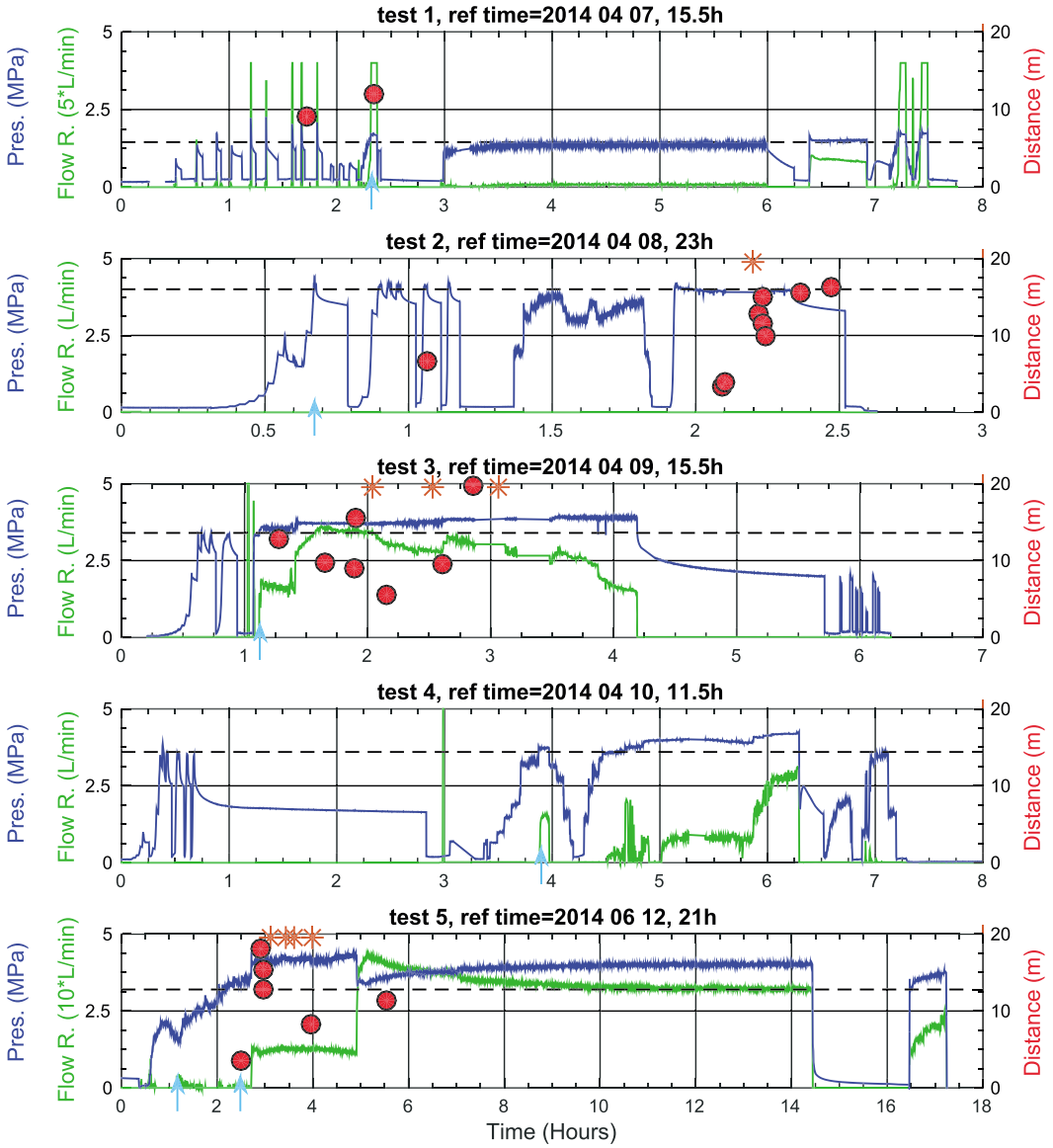

Figure 2. Injection pressure (blue lines), flow rate (green lines), and event hypocenter distance (red dots) versus time for the five injection tests. The hypocenter distance is measured from the middle (tests 1 to 4) or the beginning (test 5) of the injection chamber. The red asterisks indicate the occurring time of the events which could not be located. Note that the flow rate was not measured before 1.3 h and after 1.8 h in test 2, before 1 h in test 3, and before 3 h in test 4. The dotted lines indicate the fault opening pressure (FOP) for tests 1, 3, 4, 5, and the fracture propagation pressure (FPP) for test 2. Timings of the first failures are indicated with light blue array. From the top, downward: test 1 (reference time: 2014 May 07, 15 h30 UTC); test 2 (2014 May 08, 23 h); test 3 (2014 May 09, 15 h30); test 4 (2014 May 10, 11 h30); and test 5 (2014 May 09, 21 h).

In order to check the monitoring systems and the analysis method, we performed calibration tests, consisting of hammer shots on the tunnel walls and explosive shots (Nonel detonators) in the undamaged medium at the end of the injection borehole (outside the injection tests) and in four additional 3 m long boreholes. These tests revealed that two sensors were not properly functioning during the experiment. They also allowed us to infer the homogeneous properties of the medium, giving mean velocities for the *P* and *S* waves of 3541 m/s and 1926 m/s, respectively, and a *P* wave attenuation characterized by a quality factor of about 30. Finally, we also checked the orientation of the sensors inside the boreholes by computing the azimuth and incidence angles of the *P* waves generated by the calibration shots. The observed orientation of 8 out of the 10 working sensors are consistent (i.e., with direction differences smaller than 10°) with the theoretical orientation. We will therefore use the *P* wave polarity of the first arrival waves measured on those eight sensors in the location process.

Table 1. Summary of the Injection Tests[a]

Test Number	Date-Time	Duration	Fault Zone	Main Geological Structures	Injection Location From the Fault Core	FOP/FPP (MPa)	Max Flow Rate (L/min)	Number of Events	Maximum Displacement (mm)
1	2014/04/07-15 h	8 h	West damage zone	Polished secondary faults (N0, 80°W, Fam. 2)	~4.5 m west	1.5	12	2	0.03
2	2014/04/08-23 h	3 h	Intact host zone	Bedding (N90, 0-to10°N)	~5 m east	4.4	0.25	10	0.09
3	2014/04/09-15 h30	7 h	East damage zone	Calcified fractures (N160, 45°W, Fam 1)	~1 m east	3.3	3.8	10	0.23
4	2014/04/10-11 h	8 h	Fault core	Fault core (N0, 75°W)	Fault core	3.4	2.8	0	0.55
5	2014/06/12-20 h	18 h	Full fault zone	All	1 m west to 8 m east	2.1/3.1	43	10	X

[a]For each injection series: date/time, geological structures, location, fracture opening pressure (FOP, Test 1, 3, 4, and 5) or fracture propagating pressure (FPP, test 2), maximum flow rate, number of seismic events, and maximum displacement measured at the injection.

4. Hydromechanical Response of the Tested Zones

4.1. Fault Hydraulic Response

In test 1, injection was conducted in a polished and striated 10 m long secondary fault (Family 2), in the western damage zone. A large increase of the flow rate (8–12 L/min) occurred when the pressure was raised above 1.5 MPa (e.g., at $t = 2.29$ h in Figure 2). Such a sudden increase in the flow rate without any significant increase of pressure indicates that the tested structure is opening to accept fluid (fracture opening pressure—FOP) [*Zoback et al.,* 1980]. When the pressure fell below this value, no or limited injected flow rate was measured, showing that this opening is strongly conditioned by effective stress variations. The same hydraulic response was observed in test 3, where injection was conducted in the eastern damage zone. The flow rate increased to a maximum value of 3.8 L/min ($t = 1.1$ h). Compared to test 1, this value is threefold lower, while the opening pressure (FOP of 3.3 MPa) is twice higher. In the fault core (test 4), the flow rate significantly increased to a maximum value of 2.8 L/min when the pressure was set above 3.4 MPa ($t = 3.85$ h). Injections conducted in test 2, in the intact host rock, followed an extended leak-off test protocol [*Addis et al.,* 1998]. The first failure in the host rock was observed for a pressure of about 4.4 MPa (formation breakdown pressure, FBP; $t = 0.74$ h). Then, the fracture propagated when the pressure was raised above 4.0–4.1 MPa (fracture propagation pressure, FPP). Below 4.0 MPa, there was no water injection in the interval (for example, between 1.3 and 1.8 h, see Figure 2), while an average 0.25 L/min flow rate was injected above the FPP.

Test 5 displayed complex pressure and flow rate variations probably related to the larger injection area within the fault zone. Indeed, the different fault hydromechanical responses previously isolated in tests 1 to 4 are included in this test. Schematically, there was a first flow rate increase to approximately 4.5 L/min when the pressure was set at about 2.1 MPa ($t = 0.95$ h). This hydraulic response is close to the response of test 1. Then, a fracture opening threshold is reached at approximately 3.6 MPa ($t = 2.6$ h) at which flow rate sharply increases and then stabilizes at about 13 L/min. Flow rate then increases spontaneously to 40 L/min, and pressure drops to 3.35 MPa ($t = 4.9$ h). These pressure thresholds are close to the fault opening pressures (FOP) observed in tests 3 and 4, but the fault opening is here associated with a much higher flow rate than the one observed for tests 3 and 4. Indeed, if we sum the maximum flow rates measured at tests 3 and 4 (i.e., the flow rates in the eastern damage zone and in the fault core), we get a value of 6.6 L/min. The difference may thus correspond to the opening of the western fault damage zone. This simple estimation indicates that the western damage zone certainly is more permeable than the eastern one [*Guglielmi et al.,* 2015c].

Consequently, the hydraulic response of the fault zone appears to be characterized by a western damage zone that is more permeable than the eastern one, the fault core being less permeable than the damage zones. The higher FOP pressure measured in tests 3, 4, and 5 (values of 3.1 to 3.6 MPa) could be related to the higher strength of the sealed-with-calcite fractures, compared to the polished striated plane stimulated in test 1.

4.2. Fault Mechanical Response

Figure 3 shows polar views (i.e., horizontal projections) of displacement measured in the injection chamber. The total maximum displacements in tests 1 to 4, respectively, are 0.03, 0.09, 0.23, and 0.55 mm. Thus, for about the same injection pressure of 3.5 to 4.4 MPa, displacements magnitudes are the highest in the fault

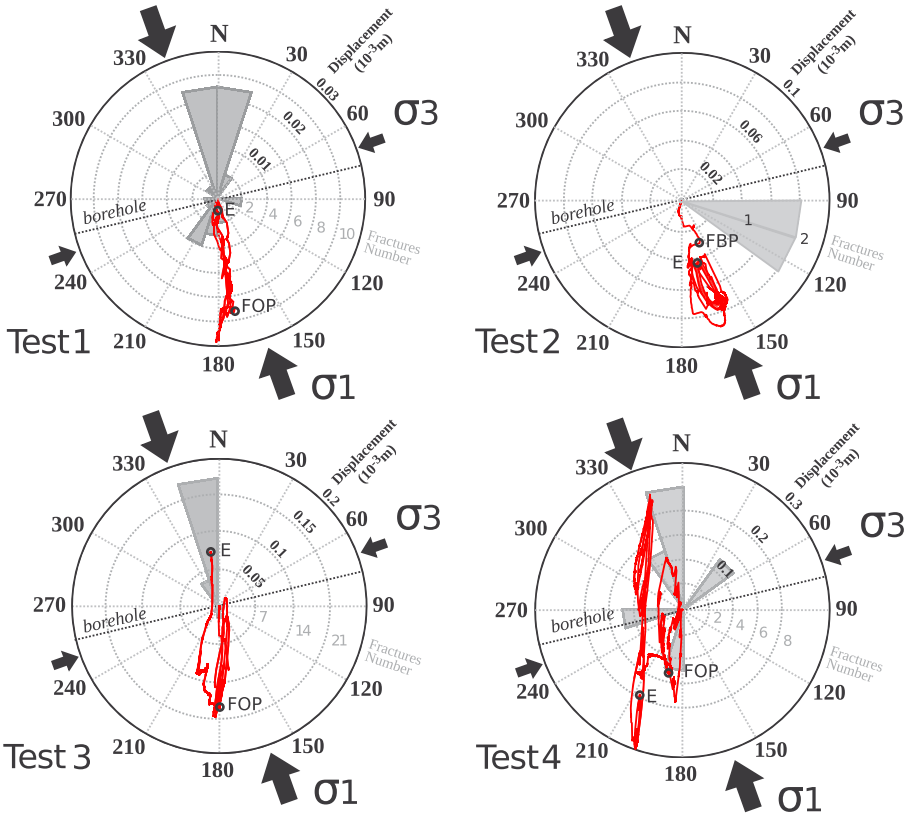

Figure 3. Polar views of the borehole displacements (red lines) measured by the SIMFIP probe (see Figure 1b) and projected onto the horizontal plane. The deformation measured at the fault opening pressure (FOP for tests 1, 3, and 4) or the fracture propagation pressure (FPP, for test 2) and the residual deformation (E) are indicated. Concentric circles figure the displacement vector magnitude variations. In gray, a rose histogram shows the density and orientation of fractures in the tested interval. Directions of the subhorizontal principal stresses σ_1 and σ_3 are figured outside the big circle (after *Cornet* [2000]). Borehole direction is figured with a dashed line.

core (test 4) and in the eastern damage zone (test 3) and the lowest in the intact rock (test 2). They are smaller in the western damage zone (test 1), where the test duration and imposed pressure were much lower. In tests 1, 3, and 4, deformation data indicate that most of the displacement corresponds to shear along the approximately N-S tested fractures. In test 2, the displacement N160 orientation follows the major horizontal stress $\sigma 1$ orientation and can be explained by shear activation along the bedding planes.

Small displacements with out-of-plane orientations occurred in all tests above the observed failures. In test 2, such reorientation occurs at the FBP point and aligns with the N72 orientation of the minimum principal stress σ_3 (see Figure 3). After the FBP, displacements produced by the following pressure cycles never returned to the initial value. N80 to 100 displacements are observed in tests 1, 3, and 4, respectively, above the fault opening pressures (FOP) of 1.43, 3.3, and 3.4 MPa (Figures 2 and 3). These displacements have magnitudes from 0.005 to 0.1 mm and can be interpreted as a normal mechanical opening of the structures tested in the intervals. Moreover, significant residual tangential displacements of 0.08 and 0.2 mm are observed along the preexisting discontinuities in tests 3 and 4. It is less clear in test 1, where the residual horizontal tangential displacement of 0.002 mm lies within instrument accuracy. In this test, this smaller inelastic component may be explained by both the shorter duration and the smaller maximum pressure applied compared to tests 3 and 4.

5. Seismicity

5.1. Events and Waveforms

Event detection was performed on the full continuous data using a Short Time Amplitude over Long Time Amplitude ratio (STA/LTA) algorithm after convolution of recordings with a set of predefined chirplets

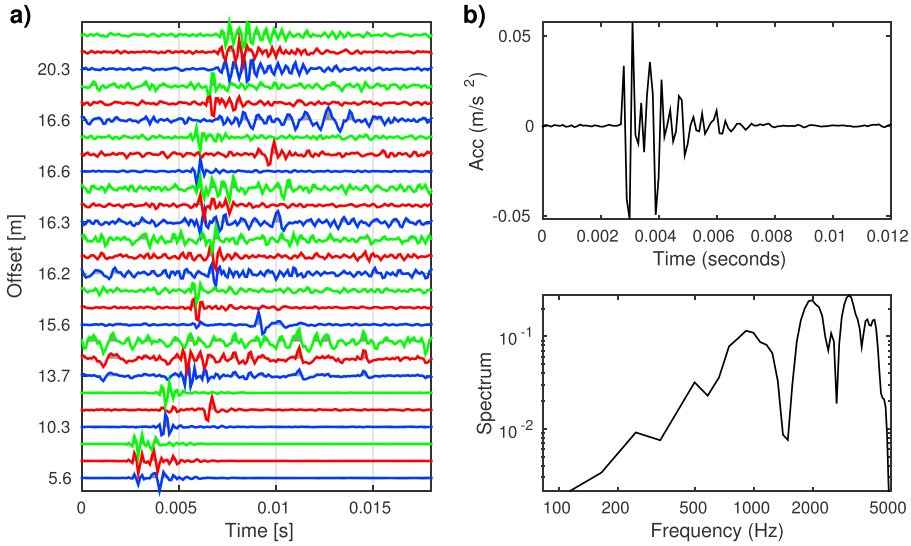

Figure 4. Waveforms of the event recorded on 2014 April 09, 17:39:25.919. (a) Waveforms versus distance. The rows with the distance label correspond to the east channels (blue), the two rows above are the north (red), and vertical (green) channels. (b) Close-up on the waveform recorded at 5.6 m from the source, north component, and its spectrum.

[*Withers et al.,* 1998]. Hundreds of events were detected, but after location we found that most of them occurred in the tunnel or close to the tunnel walls. They were discarded from this analysis as not being associated with fault responses, but rather with operations occurring in the tunnel. Twenty-seven events were classified unambiguously as events related to stress readjustments on faults/fractures. In a second passage, we increased the number of detected events performing a template matching detection [*Gibbons and Ringdal*, 2006], using a set of 9 templates among the 27 events mentioned above. We crosschecked matching candidates with a correlation coefficient greater than 0.6 on at least three receiver channels by visual inspection. A final set of 32 events was kept for the subsequent analysis.

Events were clustered in time and mainly associated with three injection tests (2, 3, and 5, see Figure 2). Only two events were identified in test 1 and none in test 4. Events only occurred at the highest pressure injection phases. For example, in test 2 (see Figure 2), events were only detected when the injection pressure was above the FPP (i.e., 4.0 MPa) but not during the 1.3 to 1.8 h injection when the injection pressure was below 4.0 MPa. Only two events were recorded after shut-in (test 2), but when the pressure was still high at the injection point. No obvious correlation between the seismicity and the flow rate has been observed. For example, tests 2 and 3, with maximum flow rate around 0.25 L/min and 3.8 L/min, respectively, induced the most seismicity, while very few events were observed during test 1 (maximum flow rate: 12 L/min) and test 4 (2.8 L/min). As tests 1 to 4 were performed within a short period of time, we cannot exclude that each test was impacting the following one. However, this would not modify the conclusions of this study.

Event waveforms clearly show *P* and *S* wave arrivals and nearly no coda at short distances (see Figure 4). Their amplitude is very small, lower than 50 mm/s^2 (or, equivalently, 1.5 μm/s in velocity) in acceleration for the largest event. These events have high-frequency contents with most of the energy above 1 kHz (see Figure 4). Because of these high frequencies and because the medium is strongly attenuating, the signal-to-noise ratio quickly decreases with distance. Most of the events vanish below the noise level (approximately 1 to 5 mm/s^2 depending on the sensors) at distances greater than 20 m.

5.2. Location

To locate the event sources, *P* and *S* wave arrivals were picked, and the polarization of the *P* wave was determined when possible. Event location was then obtained by searching for the best fit between the data (*P* and *S* waves travel times and *P* wave polarizations) and their theoretical predictions in a homogeneous medium [*Bardainne and Gaucher*, 2010]. We implemented a grid search algorithm [*Lomax et al.,* 2000] for a 3-D $80 \times 133 \times 73$ m^3 volume, with a 0.5 m grid step. We first located the calibration shots and found that the location errors were less than 2 m. Moreover, the residuals for both the calibration shots and the events

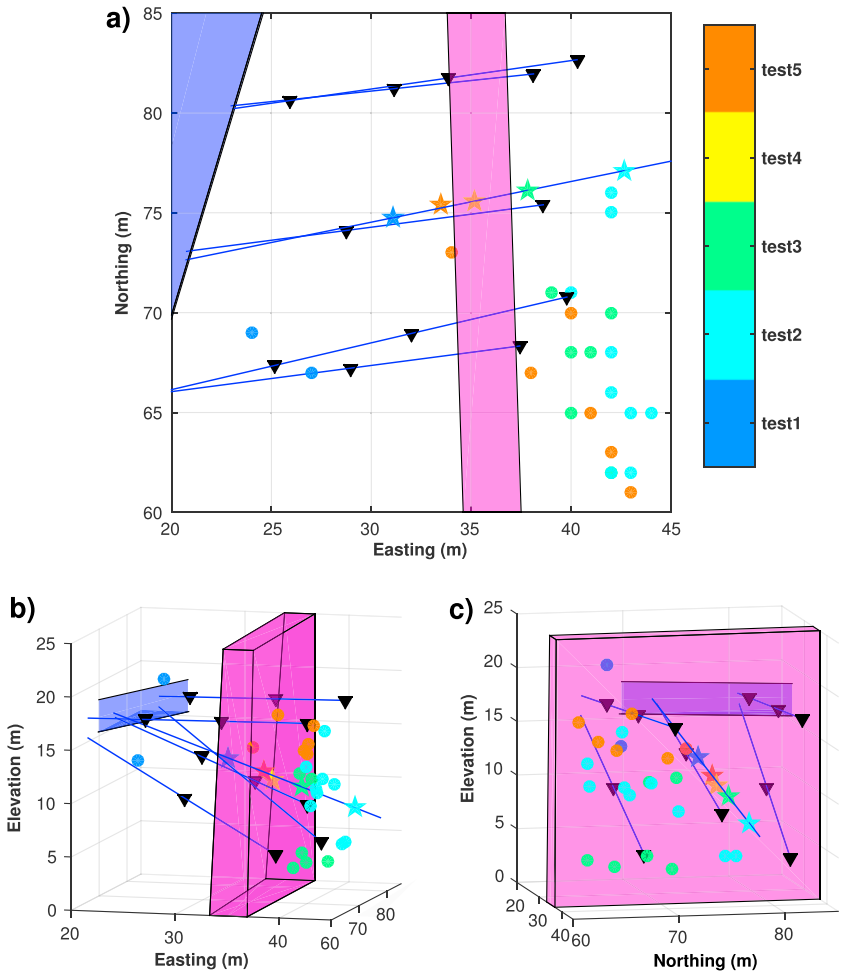

Figure 5. (a) Map view, (b) view from the south, and (c) from the east of the location of the microseismic events (dots). For the sake of simplicity, only the position of the center of the 2.4 m injection intervals for tests 1 to 4, and the beginning of the injection zone for test 5 are represented as stars. Colors refer to the test numbers. Triangles show the sensor positions, the purple area is a schematic representation of the fault core, and the blue area represents the tunnel.

lie within the same interval of ±1.5 ms for the travel times and ±10° for the polarizations. The errors found on the calibration shot location (i.e., 2 m) are therefore a good estimate of the location uncertainties. This uncertainty might seem quite large, but it takes into account both the inversion misfit and especially the assumption of a homogeneous, isotropic medium. In the following, assuming the largest error on the location (i.e., 2 m), the seismic distribution patterns we observed would still be valid.

Only 24 events had a high enough signal-to-noise ratio to be located. Most of the events are located in the eastern fault compartment, south of the injection borehole (see Figure 5). They seem to gather parallel to the fault zone, at distances smaller than 5 m from the fault core. This distribution suggests that events are populating the eastern damage zone of the fault and/or the boundary between the east damage zone and the intact rock. The east damage zone was found to be thinner than the event distribution area, but this discrepancy of thickness can be due to the lack of geological constraints on this zone and/or to the location errors. Events from tests 5 and 2 are predominantly found at higher elevations than the injection points, while the opposite is observed for test 3 events. Only three events (including the two events of the test 1) are located west of the fault core, and none are found in the core zone or north of the injections (see Figure 5).

Moreover, events are quite far from the injection points. The closest one is located 3.5 m away from the injection (test 2), and the farthest one is 19 m away (test 5). Because of the wave attenuation, we are not able to detect all events occurring at some distance from the injection. However, in the close vicinity of

the boreholes, we are highly confident that our catalog is complete at least for magnitudes above approximately −4. This means that the lack of events (or, at least, large events with $M > -4$) near the injection zones is significant.

5.3. Spectral Analysis

A spectral analysis was performed to infer the magnitude and the corner frequencies of these events. It was performed directly on the acceleration data, by fitting a ω^2 slope at low frequency and a flat response at high frequency on the Fourier spectrum of the *P* waves [*Brune*, 1970; *Boore*, 1983]. The attenuation coefficient of $Q = 30$, inferred from the calibration shots, was included in the inversion. The *P* wave radiation pattern coefficient was assumed to be 0.52 on the average values obtained from the different sensors. The errors on the magnitude associated with this assumption have been proven to range between −0.5 and +0.2 [*Daniel*, 2014]. The magnitude of these events lies between −4.2 and −3.8, with scalar moment ranging from 800 to 4500 N m. They are about one unit below the magnitudes ($M > -3$) commonly observed on reservoir monitoring [*Davies et al.*, 2013]. The *P* wave corner frequencies f_0 are found to vary from 1.5 to 2.2 kHz. Assuming a classical rupture model with a rupture velocity V_R lower than the shear wave velocity V_S ($V_R = 0.9 * V_S$), the crack radius *a* is linked to the corner frequencies f_0 by the relationships $a = 0.32 * V_S / f_0$ [*Madariaga*, 1976]. The seismic source area was found to have radii comprised between 0.2 and 0.3 m. This leads to a shear displacement on the failure plane ranging between 0.5 to 1 μm. Using the seismic moment and the crack radius [*Madariaga*, 1976], stress drops were found to be very low, ranging between 0.04 and 0.06 MPa. Note, however, that these estimates are prone to uncertainties, as a factor 2 error on the estimation of the rupture size from the corner frequency would lead to a standard value for the stress drop (approximately 1 MPa).

5.4. Source Mechanisms

The source mechanisms of 16 events were estimated from the amplitude of *P* and *S* arrivals, following the approach of *Godano et al.* [2009]. The determination of the coefficients of the moment tensor solution is performed by comparing the direct *P* and *S* wave amplitude with theoretical solutions in a simulated annealing inversion scheme (see *Godano et al.* [2009, 2011] for details on the method). Both full moment tensor and double-couple constrained mechanisms yield very consistent double-couple (DC) solutions (i.e., rake, dip, and azimuth). This, along with a good coverage of the focal sphere for individual solutions, provides us with a reasonable confidence in the stability of the DC part. Besides, isotropic and compensated linear vector dipole components are much more scattered from one event to another. They are usually small (<15%) but can reach up to 60% for some events, although waveforms do not seem so different. We therefore suspect that these non-DC components might also reveal poorly constrained degrees of freedom [*Šílený and Milev*, 2008]. We thus here focus on the double-couple constrained solutions only in our analysis, even if we cannot completely dismiss the possibility that focal mechanisms present off-plane components (i.e., transtensional mechanism).

Focal mechanisms in map view and pressure-temperature axis in vertical cross section are shown in Figure 6. Overall, the focal solutions do not reveal a single solution consistent with the stress field, even if the *P* and *T* axes (see Figure 6b) mainly show an average north-south orientation, with an approximate dip of 45° either southward or northward. There is an underlying ambiguity in discriminating which of both nodal planes is the seismic fault. Figure 7 presents the focal planes, without polarities, together with the main structures observed in the damage zones. Focal mechanisms for six events do not group together and are difficult to correlate with the geological features. This can be due to uncertainties in the mechanism determination or to an oversimplification of complex geological structures into three main fracture families. However, 10 events out of 16 (i.e., around 2/3 of the events) present one nodal plane striking from 150° to 200°, with a low dip angle, varying between 25° and 50°W. This orientation is in very good agreement with the dominant fracture orientation in the damage zones (Family 1, oriented N150–180, 30–60°W). These structures have been recognized as calcite-filled fractures and have been identified on both sides of the fault. The second nodal planes (N45–N90°, subvertical) cannot be correlated to any identified geological structures. We therefore propose that the fault planes are oriented like the existing low-dipping calcite-filled fractures, while the subvertical nodal planes are the auxiliary planes (see Figure 7b). Under this assumption, the mechanisms are dominantly strike-slip faulting (either left lateral or right lateral), with small normal or reverse components. The rake angles are indeed either between −30° and +30° or close to ±180° (see Figure 7c).

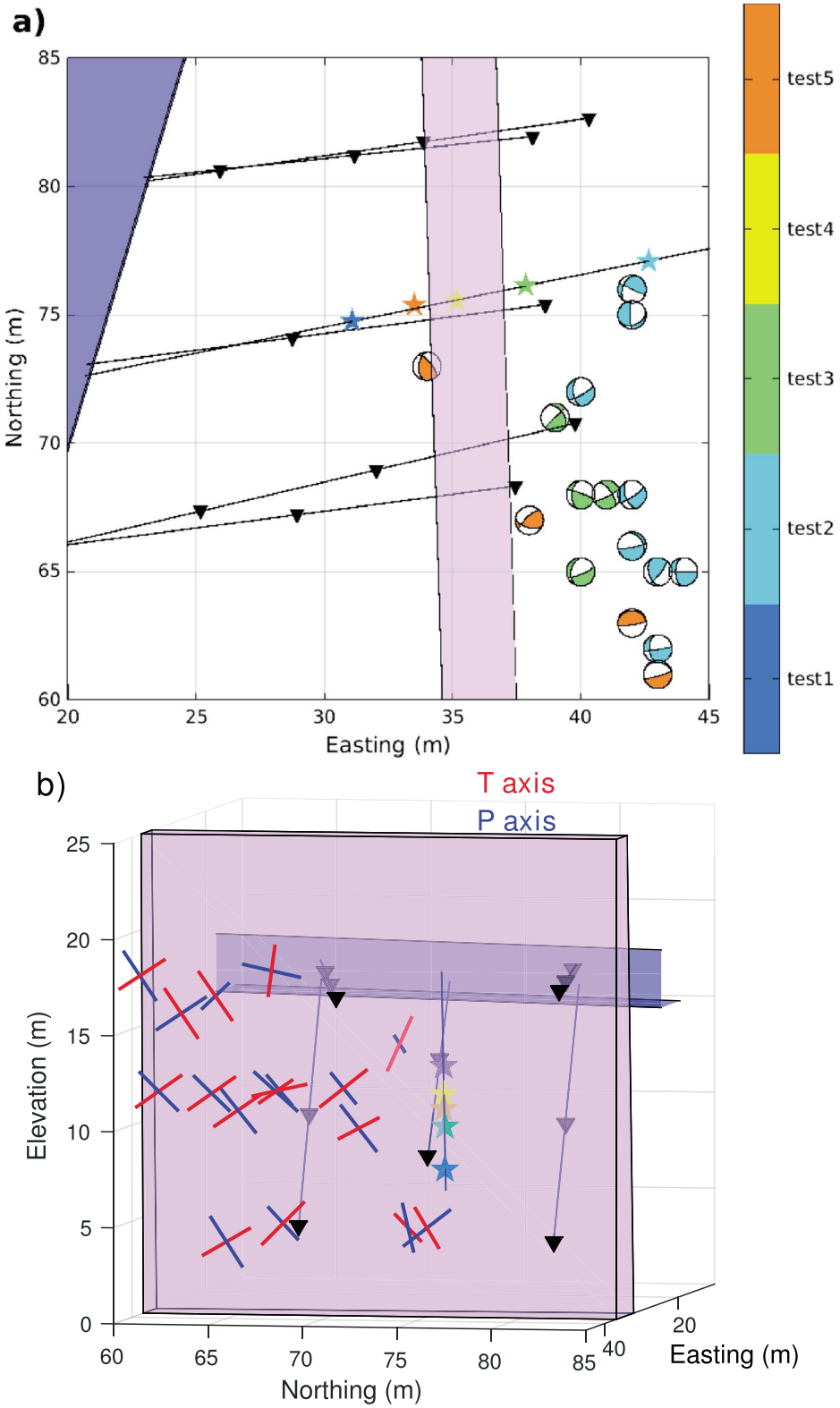

Figure 6. (a) Focal mechanisms of 16 events inferred from moment tensor inversion, in a map view. Colors show the test numbers. (b) Sub-vertical cross -section, view from the east, showing the pressure (P, blue segments) and tension (T, red segments) axes. In both panels, black triangles stand for the sensors, the blue lines are the boreholes, the purple area is a schematic representation of the fault core, and the blue area represents the tunnel. The stars indicate the center of the injection for tests 1 to 4 and the beginning of the injection zone for test 5.

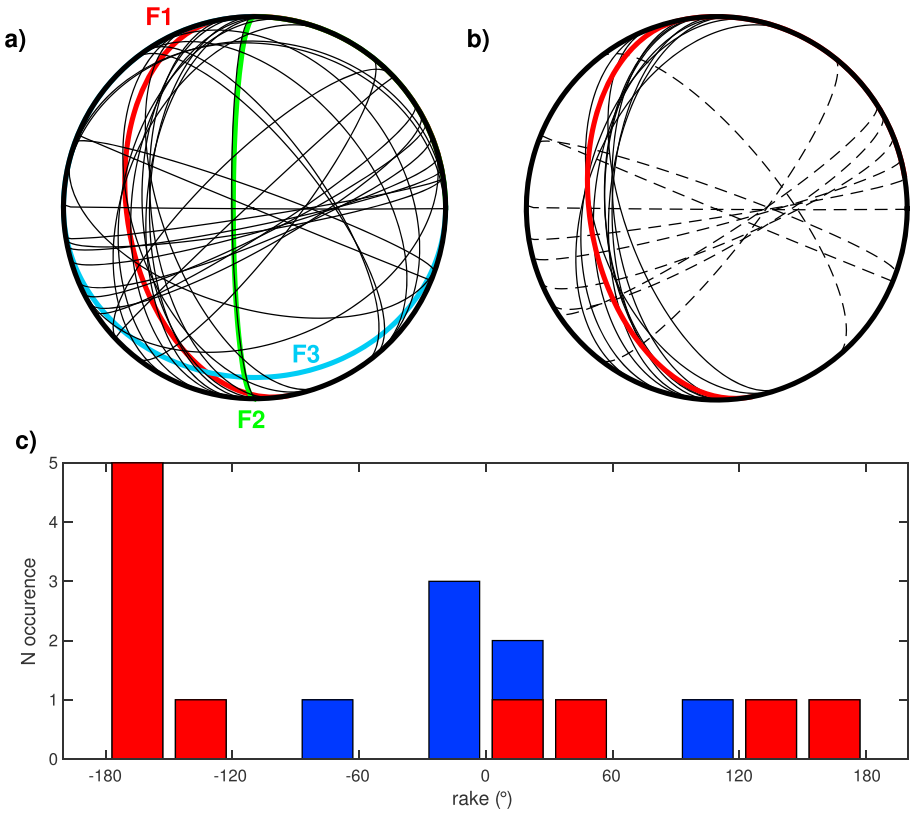

Figure 7. (a) Focal mechanisms (without polarities) of the DC constrained solutions for the 16 events, together with the structure families 1, 2, and 3 observed in the damage zone of the fault (see section 2). (b) Same as Figure 7a, but with only the 10 mechanisms, which show a similarity with the geological features. The fault traces are shown as plain lines, while the nodal planes are the dotted lines. (c) Distribution of the rakes (measured from strike) for the 16 events. Red bars are for the 10 events shown in Figure 7b, and the blue bars are the rakes of the six other events, assuming that the fault plane is the one with the lowest dip angle.

6. Discussion

6.1. Seismic Versus Aseismic Response

The response of a fault zone in shale materials was tested through five high-pressure water injections in different zones. For tests 1, 3, and 4, the displacements measured at the injection intervals show a dominantly shear failure motion on the tested faults. The measured displacements reach 30 μm (test 1) to 550 μm (test 4, see Figure 3). A sparse seismicity was observed during these injections: only 32 events were detected. These events have magnitudes smaller than −3.7 and are generated in shearing zones with a radius smaller than 0.2 m. In addition to their scarcity, these events are also very small. The cumulative seismic moment is lower than 70 kN m, equivalent to a magnitude −3 event.

Several observations support the conclusion that deformation is dominantly aseismic:

1. The total moment release by the seismic events is very small (less than 0.01%) compared to the overall deformation. The seismic deformation is inferred to be < 1 μm on surfaces < 0.1 m^2, while it is larger than 30 μm at the injection points, on much larger surfaces. The slipping patch on the tested preexisting fault was indeed estimated through hydromechanical modeling by *Guglielmi et al.* [2015b] to be about 34 m^2 for test 1. This aseismic behavior reaches its top for test 4, in the fault core, where a shearing and plastic deformation of 550 μm was measured at the injection, without any seismicity observed.
2. The seismic patches are too small and too distant between each other to form a continuous seismic structure. It is therefore likely that only a few "sticky" seismic patches are embedded in an overall aseismic deformation.
3. The distribution of the seismicity is very uneven. The location of the events is mainly confined to a particular area in the eastern damage zone, south of the injection zone, and far from the injection zones.

Therefore, deformation in the vicinity of the injection, in the core zone and west of the fault, appears to be predominately aseismic. Either fault architecture, mineralogy, stress distribution, and/or fluid pressure should explain the distribution of the seismicity.

6.2. Geological Structure, Fluid, or Stress Control?

6.2.1. Mineralogical Control

The focal mechanisms of these events show that most of them occurred on calcified fractures (Family 1) belonging to the damage zones. As shown by laboratory friction experiments performed on different shale materials [e.g., *Kohli and Zoback*, 2013] at room temperature and low-confining pressure, shale failure behavior is aseismic for large clay content, such as in the Tournemire shale. On the contrary, calcite shows an unstable failure at low temperature [e.g., *Verberne et al.,* 2014]. Therefore, this difference in frictional properties may explain why seismicity is mainly observed on fractures with calcite fillings. This assumption is consistent with the lack of seismicity during test 4: the core zone contains relatively few calcified fractures and they display less continuity. In addition, the cemented state of the fracture may allow for stress concentrations, producing localized failures on unstable slip zones [*Niemeijer and Spiers,* 2005]. However, the seismicity was mainly observed in the eastern damage zone, while the calcified fracture family is present on both sides of the fault, which were both tested. The presence of an adequate mineralogy does not explain the asymmetric distribution of the seismicity.

6.2.2. Fluid-Flow Control

No seismicity is recorded in the close vicinity of the injections. Several possibilities might explain this:

1. A lack of calcified fractures in these areas. However, injection in test 3 directly occurred in such fractures. A shearing failure is observed at the injection point, with a displacement of 0.2 mm, but no seismicity was recorded at distances less than 6 m (see Figure 2).
2. A significant fracture opening preceding or accompanying the shear deformation. Tensile openings have a slower rupture velocity than shear failure [*Broberg*, 2006], which can lead to aseismic or nearly aseismic behavior. However, the deformation of test 3 shows that above the FOP, the shear failure is predominant.
3. A reduction of the frictional properties by water, for both shale and calcite [*Verberne et al.,* 2014; *Morrow et al.,* 2000; *Moore and Lockner*, 2004], which potentially leads to stable deformations.
4. Planes misoriented with the stress field. Such planes cannot slip without a strong decrease of the effective stress. This prevents a fast velocity rupture, as the slip cannot be faster than the pressure diffusion on the plane [e.g., *Zoback et al.,* 2012].

Under these different possibilities, the presence of fluid would not favor seismicity in the vicinity of the injection. The seismicity is therefore likely to be localized outside or at the extremities of the area with injected water. This is in good agreement with the results of another experiment of fault activation in carbonates [*Guglielmi et al.,* 2015a], which shows that slips in the pressurized zone are slow and aseismic.

Seismicity only occurred at high pressures, i.e., at pressures above the measured fault opening pressures (FOP) of 3.1–3.5 MPa. Several limited-rate water outflows were observed during the experiments, through the tunnel walls and the boreholes. They are only localized south of the injections. This may show that water mostly propagated southward and therefore explains why seismicity was only located southward.

6.2.3. Fault Structure and Stress Transfer

As both sides of the faults were tested, a difference in the stress transfer, in relation to the fault structure, should exist. The heterogeneities of mechanical properties across the fault zone may modify the stress field distribution, which is then far more complex than a homogeneous field at a very local scale. In particular, the fault structure may lead to a rotation of the stress direction in the damage zones [*Faulkner et al.,* 2006]. However, with the exception of test 1, fault opening pressures are similar in the two fault compartments. If we consider that tested structures in both compartments have a similar N0 orientation, we can thus conclude that the stress state is likely to be the same in both compartments. Moreover, from the analysis of pressure-displacement data of test 1, *Guglielmi et al.* [2015b] determined a stress state identical to the regional stress obtained by *Cornet* [2000]. Therefore, the tunnel has a weak effect on the stress even for test 1.

The hydraulic structure of the fault zone is also heterogeneous. For a similar FOP, the injected flow rate is much higher in the western fault damage zone (test 5) than in the eastern damage zone (test 3 + test 4).

The 10 m scale secondary faults of Family 2 are only present in the western compartment, while only short length fractures, less connected, exist east of the fault. *Guglielmi et al.* [2015c] show that the permeability is therefore higher in the western compartment than in the eastern one. In addition, as only few fractures cross the fault core, this zone is less permeable than the surrounding damage zone. Therefore, the fault can also act as a fluid barrier and "trap" fluids in the eastern damage zone, where the low permeability would favor an increase in pressure in a larger body. Conversely, in the western damage zone, higher permeability and the tunnel acting as a zero potential permeable boundary may favor fluid drainage. Therefore, for a similar fluid pressure at the injection on both sides of the fault, the fluid pressure can diffuse to a larger distance in the eastern compartment. Therefore, the volumetric dilatation (by fracture openings and poroelastic deformation) will extend further, leading to a larger stress perturbation transferred outside the injected area. More seismic events will be generated if adequate structures are present.

6.3. Analogies With Reservoir and Tectonic Zone Seismicity

The seismicity distribution in shale materials depends on (1) the mineralogy, as seismic events occurred in zones with crystallized fillings; (2) the fluids, as the presence of water seems to prevent the seismicity, but the fluid pressure induces (3) a stress transfer, which is sensitive to the structural and hydromechanical properties of the fault. These observations may have strong impacts on the monitoring of reservoirs or seismogenic fault zones.

Indeed, for reservoir monitoring, the overall seismicity does not seem to be a direct probe for the fluid flow, as it depends on several structural properties. First, little or no seismicity will be recorded if the mineralogy is not compatible with a seismic behavior. This is consistent with laboratory experiments [e.g., *Ikari et al.,* 2009; *Kohli and Zoback,* 2013] which show a stable slip behavior in shale. The number of events and their distribution can therefore be a proxy for the presence of recrystallized structures rather than an indication on the fluid distribution. For instance, *Eaton et al.* [2013] studied the seismicity recorded in the Montney reservoir and the differences of its seismic responses (mainly numbers and types of seismic events) with the Barnett shale reservoirs [*Das and Zoback,* 2013a, 2013b] by comparing the density and the complexity of the fractures in those reservoirs.

Second, the irregularity in the seismicity distribution can map the stress transfer heterogeneities rather than the fluid location. The heterogeneous hydromechanical properties across the fault zone might modify how the stress transferred from the pressure. Such asymmetric patterns in the seismicity distribution have been observed by, for example, *Maxwell and Norton* [2012] in the Montney reservoir. In a similar way, *Andersen et al.* [2013] showed that the microseismicity in shale depends on the overall stress state and the presence of heterogeneities (e.g., fractures) rather than on the brittleness of the materials. *Rutledge et al.* [2004] also observed that the areas of stress concentrations in the Carthage Cotton Valley reservoir are more prone to generate high-level seismicity. Structural heterogeneities, leading to heterogeneous stress transfer from the pressure, should therefore be accounted for with care when monitoring seismicity, as they may mask the fluid flow in the seismicity distribution.

Some analogies can be drawn between these experimental results and large faults with a weak core, i.e., containing some amount of clay. Wet clays show a velocity-strengthening behavior [*Bullock et al.,* 2015], leading to aseismic slips, with little energy required to maintain rupture propagation [*Faulkner et al.,* 2011]. Such behavior has been observed in different tectonic settings, such as low-dipping normal faults [e.g., *Tesei et al.,* 2014], subduction areas [e.g., *Faulkner et al.,* 2011; *Vallée et al.,* 2013], or transform faults [e.g., part of the San Andreas fault, *Carpenter et al.,* 2011]. As the main deformation is aseismic, the seismicity only represents a small percentage of the moment release [*Das and Zoback*, 2013a, 2013b; *Vallée et al.,* 2013]. Thus, the seismicity is only an accommodation response of the stable slip on localized seismic surfaces embedded on the fault or in its vicinity. The complex internal structures of faults may lead to stress concentrations around geometric irregularities with higher frictional properties, such as lenses of more intact rocks, topographical asperities, or veins of recrystallized structures [*Lay and Kanamori*, 1981; *Niemeijer and Spiers*, 2005; *Chen and Lapusta*, 2009; *Vallée et al.,* 2013]. The seismicity may also occur in the vicinity of the main fault, on secondary faults with unstable frictional behavior [*Rubin et al.,* 1999; *Guglielmi et al.,* 2015a]. This has been observed, for example, in central Italy [*Collettini and Barchi,* 2002], where a low-angle normal fault aseismically slips and induces seismicity in the formation above. Asymmetric distribution of the seismicity has been

observed on faults which separate different rock bodies [e.g., *Powers and Jordan*, 2010; *Zaliapin and Ben Zion,* 2011 on Californian faults]. This asymmetry is explained as a difference in the mechanical properties across the fault. Similarly, the asymmetric distribution of the seismicity we observed seems due to a difference in the mechanical, but also hydrological, properties.

Even if the pressure, temperature, geometry, and scale of this experiment differ from the conditions observed in a tectonic context, analogies can be drawn with reservoirs and tectonic zones, as the full complexity of a fault zone is represented here. It highlights the importance of the hydromechanical properties of the internal structure of the faults in the distribution of the seismicity.

7. Conclusion

An in situ experiment was performed at an intermediate scale (approximately 10 m). High pressure water was injected in different areas of a natural fault zone located in a shale material. The scale of this experiment allows a detailed description of the geological structures and the installation of sensors in the close vicinity of the tests. This study focuses on the induced seismicity in the light of a well-known geological and hydromechanical context. Only a sparse seismicity was recorded, which shows that most of the deformation is aseismic. We therefore observed aseismic and seismic behavior, i.e., quasi-static and fast failures, but we did not see any clear seismic evidence for intermediate behavior (i.e., slow failures), which can be expressed seismically as long-period long duration events [*Das and Zoback,* 2013a, 2013b; *Zecevic et al.,* 2016] or tremor signals [*Derode et al.,* 2015; *Peng and Gomberg*, 2010].

The locations and focal mechanisms of the seismicity reveal an asymmetric distribution, which allows us to discuss the parameters controlling the seismic or aseismic behavior in shale materials. As the seismicity mainly occurred on calcified structures, the number of events might depend on the density of such fractures. The fault zone acts as a fluid barrier and shows heterogeneous hydromechanical properties. This likely induces modifications on how the stress is transferred from the pressure buildup. This heterogeneity seems to be the main controlling factor for the seismic source distribution. From a monitoring point of view, it means that seismic emissions cannot be directly linked to the fluid flow, but rather to the internal properties of the fault architectures.

Acknowledgments

This work has been supported by the TOTAL Company within the framework of the "Fluids and Faults" project, whose PIs are Claude Gout, Raymi Castilla (Total), and Pierre Henry (Cerege, Aix Marseille University). The authors thank the IRSN (French Institute of Radioprotection and Nuclear Safety) for providing their dedicated help and access to the IRSN Tournemire underground laboratory. We also deeply thank Patrice Desveaux who ensured that everything worked on the site. The SIMFIP device has been codeveloped by the CEREGE, SITES SAS, and Petrometalic companies under cofunding from the ADEME (French Agency of Environment and Energy). We thank J. Durand and Y. Zouhair (SITES engineers) for installing and maintaining the sensors and acquisition during the experiments. OSU Pytheas (Aix Marseille University) helped us for the on-site storage and the data transfer of the 30 To of data recorded during the experiment. We thank the Magnitude Company (Sainte-Tulle, France office) for microseismic data processing (amplitude detection, location, and mechanisms). All experimental data are stored in the Géoazur laboratory, CNRS, University Nice Sophia-Antipolis, and are available upon request (contact louis.debarros@geoazur.unice.fr).

References

Addis, M. A., T. H. Hansen, N. Yassir, D. R. Willoughby, and J. Enever (1998), A comparison of leak-off test and extended leak-off test data for stress estimation, *SPE/ISRM*, *1*, 1–2.

Andersen, E., H. Davey, C. Steinhoff, and T. Davis (2013), Investigating the relationship between microseismic events and geomechanical variations in the Montney Shale reservoir—A case study, *First Break*, *31*(2), 71–77.

Bardainne, T., and E. Gaucher (2010), Constrained tomography of realistic velocity models in microseismic monitoring using calibration shots, *Geophys. Prospect.*, *58*(5), 739–753.

Bodziak, R., K. Clemons, A. Stephens, and R. Meek (2014), The role of seismic attributes in understanding the hydraulically fracturable limits and reservoir performance in shale reservoirs: An example from the Eagle Ford Shale, south Texas, *AAPG Bull.*, *98*(11), 2217–2235.

Boore, D. M. (1983), Stochastic simulation of high-frequency ground motions based on seismological models of the radiated spectra, *Bull. Seismol. Soc. Am.*, *73*(6A), 1865–1894.

Broberg, K. B. (2006), Differences between Mode I and Mode II crack propagation, *Pure Appl. Geophys.*, *163*, 1867–1879.

Brune, J. N. (1970), Tectonic stress and the spectra of seismic shear waves from earthquakes, *J. Geophys. Res.*, *75*, 4997–5009, doi:10.1029/JB075i026p04997.

Bullock, R. J., N. De Paola, and R. E. Holdsworth (2015), An experimental investigation into the role of phyllosilicate content on earthquake propagation during seismic slip in carbonate faults, *J. Geophys. Res. Solid Earth*, *120*, 3187–3207, doi:10.1002/2015JB011914.

Carpenter, B. M., C. Marone, and D. M. Saffer (2011), Weakness of the San Andreas Fault revealed by samples from the active fault zone, *Nat. Geosci.*, *4*(4), 251–254.

Charpentier, D., D. Tessier, and M. Cathelineau (2003), Shale microstructure evolution due to tunnel excavation after 100 years and impact of tectonic paleo-fracturing. Case of Tournemire, France, *Eng. Geol.*, *70*(1), 55–69.

Chen, T., and N. Lapusta (2009), Scaling of small repeating earthquakes explained by interaction of seismic and aseismic slip in a rate and state fault model, *J. Geophys. Res.*, *114*, B01311, doi:10.1029/2008JB005749.

Collettini, C., and M. R. Barchi (2002), A low-angle normal fault in the Umbria region (central Italy): A mechanical model for the related microseismicity, *Tectonophysics*, *359*(1), 97–115.

Constantin, J., J. B. Peyaud, P. Vergély, M. Pagel, and J. Cabrera (2004), Evolution of the structural fault permeability in argillaceous rocks in a polyphased tectonic context, *Phys. Chem. Earth*, *29*, 25–41.

Cornet, F. H. (2000), Détermination du champ de contrainte au voisinage du laboratoire souterrain de Tournemire, *Rapp. N°98 N33/0073*, Rapp. du Lab. de Méc. des Roches, Dép. de Sismol., Inst. de Phys. du Globe de Paris.

Daniel, G. (2014), Bias in magnitude for earthquakes with unknown focal mechanism, *Geophys. Prospect.*, *62*, 848–861.

Das, I., and M. Zoback (2013a), Long-period, long-duration seismic events during hydraulic stimulation of shale and tight-gas reservoirs—Part 1: Waveform characteristics, *Geophysics*, *78*(6), KS107–KS118.

Das, I., and M. Zoback (2013b), Long-period long-duration seismic events during hydraulic stimulation of shale and tight gas reservoirs—Part 2: Location and mechanisms, *Geophysics*, *78*(6), KS97–KS105.
Davies, R., G. Foulger, A. Bindley, and P. Styles (2013), Induced seismicity and hydraulic fracturing for the recovery of hydrocarbons, *Mar. Pet. Geol.*, *45*, 171–185.
Den Hartog, S. A. M., and C. J. Spiers (2013), Influence of subduction zone conditions and gouge composition on frictional slip stability of megathrust faults, *Tectonophysics*, *600*, 75–90.
Derode, B., Y. Guglielmi, L. De Barros, and F. Cappa (2015), Seismic responses to fluid pressure perturbations in a slipping fault, *Geophys. Res. Lett.*, *42*, 3197–3203, doi:10.1002/2015GL063671.
Dick, P., C. Courbet, C. Wittebroodt, A. Dauzeres, and J.-M. Matray (2015), Internal structures of fault zones in low permeability formations and their relationship with fluid flow: insights from the Tournemire URL, paper presented at Clay Conference, Brussel, Belgium.
Eaton, D. W., M. van der Baan, J.-B. Tary, B. Birkelo, N. Spriggs, S. Cutten, and K. Pike (2013), Broadband microseismic observations from a Montney hydraulic fracture treatment, northeastern B.C., Canada, *CSEG Rec.*, *38*, 44–54.
Faulkner, D. R., T. M. Mitchell, D. Healy, and M. J. Heap (2006), Slip on weak faults by the rotation of regional stress in the fracture damage zone, *Nature*, *444*(7121), 922–925.
Faulkner, D. R., M. Mitchell, J. Behnsen, T. Hirose, and T. Shimamoto (2011), Stuck in the mud? Earthquake nucleation and propagation through accretionary forearcs, *Geophys. Res. Lett.*, *38*, L18303, doi:10.1029/2011GL048552.
Gibbons, S. J., and F. Ringdal (2006), The detection of low magnitude seismic events using array-based waveform correlation, *Geophys. J. Int.*, *165*(1), 149–166.
Godano, M., M. Regnier, A. Deschamps, T. Bardainne, and E. Gaucher (2009), Focal mechanisms from sparse observations by nonlinear inversion of amplitudes: Method and tests on synthetic and real data, *Bull. Seismol. Soc. Am.*, *99*(4), 2243–2264.
Godano, M., T. Bardainne, M. Regnier, and A. Deschamps (2011), Moment tensor determination by nonlinear inversion of amplitudes, *Bull. Seismol. Soc. Am.*, *101*(1), 366–378.
Guglielmi, Y., F. Cappa, H. Lançon, J. Janowczyk, J. Rutqvist, C. Tsang, and J. Wang (2013), ISRM suggested method for step-rate injection method for fracture in-situ properties (SIMFIP): Using a 3-components borehole deformation sensor, *Rock. Mech. Rock Eng.*, *47*, 303–311.
Guglielmi, Y., F. Cappa, J. F. Avouac, P. Henry, and D. Elsworth (2015a), Seismicity triggered by fluid injection-induced aseismic slip, *Science*, *348*(6240), 1224–1226.
Guglielmi, Y., D. Elsworth, F. Cappa, P. Henry, C. Gout, P. Dick, and J. Durand (2015b), In situ observations on the coupling between hydraulic diffusivity and displacements during fault reactivation in shales, *J. Geophys. Res. Solid Earth*, *120*, 7729–7748, doi:10.1002/2015JB012158.
Guglielmi, Y., P. Henry, C. Gout, and P. Dick (2015c), Field experiments of fault activation in shales, paper 767 presented at Shale Symposium, 13th International Congress of Rock Mechanics, Montréal, Canada.
Heermance, R., Z. K. Shipton, and J. P. Evans (2003), Fault structure control on fault slip and ground motion during the 1999 rupture of the Chelungpu fault, Taiwan, *Bull. Seismol. Soc. Am.*, *93*(3), 1034–1050.
Ikari, M. J., D. M. Saffer, and C. Marone (2009), Frictional and hydrologic properties of clay-rich fault gouge, *J. Geophys. Res.*, *114*, B05409, doi:10.1029/2008JB006089.
Imber, J., R. E. Holdsworth, S. A. F. Smith, S. P. Jefferies, and C. Collettini (2008), Frictional-viscous flow, seismicity and the geology of weak faults: A review and future directions, *Geol. Soc. London Spec. Publ.*, *299*(1), 151–173.
Ingram, G. M., and J. L. Urai (1999), Top-seal leakage through faults and fractures: The role of mudrock properties, *Geol. Soc. London Spec. Publ.*, *158*(1), 125–135.
Kohli, A. H., and M. D. Zoback (2013), Frictional properties of shale reservoir rocks, *J. Geophys. Res. Solid Earth*, *118*, 5109–5125, doi:10.1002/jgrb.50346.
Lay, T., and H. Kanamori (1981), An asperity model of large earthquake sequences, in *Earthquake Prediction*, pp. 579–592, AGU, Washington, D. C.
Lefevre, M. (2016), Propriétés structurales, pétro-physiques et circulations de fluides au sein d'une zone de failles dans les argiles, PhD Thesis, Aix-Marseille Univ., April 26.
Lomax, A., J. Virieux, P. Volant, and C. Berge (2000), Probabilistic earthquake location in 3D and layered models: Introduction of a Metropolis-Gibbs method and comparison with linear locations, in *Advances in Seismic Event Location*, edited by C. H. Thurber and N. Rabinowitz, pp. 101–134, Kluwer, Amsterdam.
Madariaga, R. (1976), Dynamics of an expanding circular fault, *Bull. Seismol. Soc. Am.*, *66*, 639–666.
Maxwell, S., and M. Norton (2012), Enhancing shale gas reservoir characterization using hydraulic fracture microseismic data, *First Break*, *30*(2), 95–101.
Mazzoldi, A., A. P. Rinaldi, A. Borgia, and J. Rutqvist (2012), Induced seismicity within geological carbon sequestration projects: Maximum earthquake magnitude and leakage potential from undetected faults, *Int. J. Greenhouse Gas Control*, *10*, 434–442.
Moore, D. E., and D. A. Lockner (2004), Crystallographic controls on the frictional behavior of dry and water saturated sheet structure minerals, *J. Geophys. Res.*, *109*, B03401, doi:10.1029/2003JB002582.
Morrow, C. A., D. E. Moore, and D. A. Lockner (2000), The effect of mineral bond strength and adsorbed water on fault gouge frictional strength, *Geophys. Res. Lett.*, *27*, 815–818, doi:10.1029/1999GL008401.
Niemeijer, A. R., and C. J. Spiers (2005), Influence of phyllosilicates on fault strength in the brittle-ductile transition: Insights from rock analogue experiments, *Geol. Soc. London Spec. Publ.*, *245*(1), 303–327.
Peng, Z., and J. Gomberg (2010), An integrated perspective of the continuum between earthquakes and slow-slip phenomena, *Nat. Geosci.*, *3*, 599–607.
Powers, P. M., and T. H. Jordan (2010), Distribution of seismicity across strike-slip faults in California, *J. Geophys. Res.*, *115*, B05305, doi:10.1029/2008JB006234.
Rubin, A. M., D. Gillard, and J.-L. Got (1999), Streaks of microearthquakes along creeping faults, *Nature*, *400*, 635–641.
Rutledge, J. T., W. S. Phillips, and M. J. Mayerhofer (2004), Faulting induced by forced fluid injection and fluid flow forced by faulting: An interpretation of hydraulic-fracture microseismicity, Carthage Cotton Valley gas field, Texas, *Bull. Seismol. Soc. Am.*, *94*(5), 1817–1830.
Rutqvist, J., A. P. Rinaldi, F. Cappa, and G. J. Moridis (2013), Modeling of fault reactivation and induced seismicity during hydraulic fracturing of shale-gas reservoirs, *J. Pet. Sci. Eng.*, *107*, 31–44.
Saffer, D. M., and C. Marone (2003), Comparison of smectite-and illite-rich gouge frictional properties: Application to the updip limit of the seismogenic zone along subduction megathrusts, *Earth Planet. Sci. Lett.*, *215*(1), 219–235.
Shapiro, S. A., and C. Dinske (2009), Fluid-induced seismicity: Pressure diffusion and hydraulic fracturing, *Geophys. Prospect.*, *57*(2), 301–310.
Šílený, J., and A. Milev (2008), Source mechanism of mining induced seismic events—Resolution of double couple and non double couple models, *Tectonophysics*, *456*(1), 3–15.

Tesei, T., C. Collettini, M. R. Barchi, B. M. Carpenter, and G. Di Stefano (2014), Heterogeneous strength and fault zone complexity of carbonate-bearing thrusts with possible implications for seismicity, *Earth Planet. Sci. Lett.*, *408*, 307–318.

Tremosa, J., D. Arcos, J. Matray, F. Bensenouci, E. C. Gaucher, C. Tournassat, and J. Hadi (2012), Geochemical characterization and modelling of the Toarcian/Domerian porewater at the Tournemire underground research laboratory, *Appl. Geochem.*, *27*, 1417–1431.

Vallée, M., et al. (2013), Intense interface seismicity triggered by a shallow slow slip event in the Central Ecuador subduction zone, *J. Geophys. Res. Solid Earth*, *118*, 2965–2981, doi:10.1002/jgrb.50216.

Verberne, B. A., C. J. Spiers, A. R. Niemeijer, J. H. P. De Bresser, D. A. M. De Winter, and O. Plümper (2014), Frictional properties and microstructure of calcite-rich fault gouges sheared at sub-seismic sliding velocities, *Pure Appl. Geophys.*, *171*(10), 2617–2640.

Withers, M., R. Aster, C. Young, J. Beiriger, M. Harris, S. Moore, and J. Trujillo (1998), A comparison of select trigger algorithms for automated global seismic phase and event detection, *Bull. Seismol. Soc. Am.*, *88*(1), 95–106.

Zaliapin, I., and Y. Ben-Zion (2011), Asymmetric distribution of aftershocks on large faults in California, *Geophys. J. Int.*, *185*(3), 1288–1304.

Zecevic, M., G. Daniel, and D. Jurick (2016), On the nature of long-period long-duration seismic events detected during hydraulic fracturing, *Geophysics*, *81*(3), KS109–KS117.

Zoback, M. D. (2010), *Reservoir Geomechanics*, 459 pp., Cambridge Univ. Press, Cambridge, U. K.

Zoback, M. D., H. Tsukahara, and S. Hickman (1980), Stress measurements at depth in the vicinity of the San Andreas fault: Implications for the magnitude of shear stress at depth, *J. Geophys. Res.*, *85*, 6157–6173, doi:10.1029/JB085iB11p06157.

Zoback, M. D., A. Kohli, I. Das, and M. McClure (2012), The importance of slow slip on faults during hydraulic fracturing of a shale gas reservoirs, paper SPE 155476 presented at SPE Americas Unconventional Resources Conference, Pittsburgh, Pa.